Supplementary Information (SI) for Green Chemistry.

Supplementary Information

Sustainable Electrosynthesis of Hydroxymethanesulfonate from CO_2 and Sulfite

Mengjie Liu,[1,†] Aimin Li,[1,2,†] Hsiwen Wu,[1] Alan M. Bond,[1] and Jie Zhang[1,3,4,*]

[1] School of Chemistry, Monash University, Clayton, Victoria 3800, Australia

[2] State Key Laboratory of Chemo and Biosensing, College of Chemistry and Chemical Engineering, Hunan University, Changsha 410082, China

[3] ARC Research Hub for Carbon Utilisation and Recycling, Monash University, Clayton, VIC 3800, Australia

[4] ARC Centre of Excellence for Green Electrochemical Transformation of Carbon Dioxide, Monash University, Clayton, VIC 3800, Australia

† These authors contributed equally to this work.

* Corresponding Authors: Jie Zhang: jie.zhang@monash.edu

Table of Contents

Materials and methods

Chemicals and materials:

Cobalt phthalocyanine (CoPc, Sigma-aldrich), nickel phthalocyanine (NiPc, Sigma-aldrich), copper phthalocyanine (CuPc, Sigma-aldrich), carbon nanotubes (CNT, DAZHAN NAMI), *N,N*-Dimethylformamide (DMF, Ajax-finechem), Perfluorosulfonic acid (PFSA) dispersion (D20, 20%, Fuelcell store), carbon paper (Toray Paper 060), sodium sulfite (Na_2SO_3, Sigma-aldrich), sodium sulfate (Na_2SO_4, Sigma-aldrich), lithium sulfate (Li_2SO_4, Sigma-aldrich), potassium sulfate (K_2SO_4, Sigma-aldrich), cesium sulfate (Cs_2SO_4, Sigma-aldrich), sodium bisulfite ($NaHSO_3$, Sigma-aldrich). The deionized (DI) water (18.25 $M\Omega \cdot cm^{-1}$) was used in all experiments.

Characterization

Scanning electron microscopy (SEM) characterizations were performed using a JOEL 800. ^1H NMR spectra were collected using a Bruker 400 MHz instrument. Gas chromatography (GC) spectra were collected using an Agilent 7820A instrument. Ion chromatography (IC) spectra were performed using an Thermo Dionex ICS-6000.

Inductively coupled plasma mass spectrometry (ICP-MS) results were obtained from PerkinEImer NexlON 2000. Synchrotron X-ray absorption spectroscopy (XAS) measurements were performed at the Australian Synchrotron (part of the ANSTO) in Melbourne. The samples were measured using fluorescence measurements and probed from 6.3 to 19 keV above the edge. CoPc has been measured simultaneously as a reference.

Preparation of MPc/CNT (M = Co, Ni, Cu) electrodes

To prepare the catalyst ink, 2.0 mg of metal phthalocyanines (MPcs, M = Co, Cu, Ni) and 18 mg of multi-walled carbon nanotubes (CNTs) were dispersed in 20 mL of DMF containing 0.20 mL of a 20 wt% PFSA solution. This suspension was stirred magnetically at 800 rpm for 24 h at room temperature to ensure a homogeneous dispersion. For electrode fabrication, 200 μL of the resulting ink was drop-cast onto a piece of carbon paper (with a defined area of 1.0 cm × 1.0 cm). The remaining area of the carbon paper was masked with insulating tape. The ink was applied in 20 µL aliquots using a pipette (Figure S1a). During the dispensing process, the carbon paper was on a heating plate at approximately 50°C to promote slow and uniform solvent evaporation. Finally, the electrode was dried at room temperature for 24 h. The prepared catalyst-coated carbon paper was fixed on a Pt electrode holder (Figure S1b).

Electrochemical measurements

An electrochemical workstation (CHI 760E) was used to perform all electrochemical measurements. A three-electrode setup was employed in an H-type cell, where the prepared catalyst-coated carbon paper fixed on a Pt electrode holder is used as the working electrode, an Ag/AgCl electrode (Saturated KCl solution as the chloride source) served as the reference electrode, and IrO_2-supported on titanium mesh provided the counter electrode. Molecular sieves served as membranes in the H-type cell to separate the cathode and anode chambers. Each chamber was filled with 10 mL of electrolyte. All potentials reported herein are referenced to the reversible hydrogen electrode (RHE) according to the equation:

$$E_{RHE} = E_{Ag/AgCl} + 0.0591 \times pH + 0.197\ V$$

During testing, N_2/CO_2 was continuously introduced into the cathode electrolyte at a rate of 20 mL min^{-1}. The testing procedure was as follows: First, the counter electrode was activated by using cyclic voltammetry (CV) under N_2 atmosphere within the potential range of -0.8 to -1.5 V_{RHE} with a scan rate of 100 mV s^{-1}. Activation was regarded as complete when the CV date from the two consecutive cycles perfectly overlap. N_2 is then replaced with CO_2, which is continuously introduced for 30 min to give a CO_2 saturated the electrolyte. LSV testing was then performed at a scan rate of 5 mV s^{-1} until the scans converge. Subsequently, i-t data was collected under constant potential electrolysis conditions. After each experiment, the electrolyte was refreshed and CO_2 was reintroduced until saturation was achieved before the next measurement. During electrolysis at each potential, the charge (Q) was determined. The different components in experimental configuration are shown in Figure S3.

The electrochemical utilization efficiency (η%) of CoPc was calculated by comparing the actual amount of electrochemically active Co centers with the total CoPc loading:

$$\eta\% = \frac{n_{actual}}{n_{theoretical}} \times 100\% = \frac{\left(\frac{Q_{cv}}{zF}\right)}{\left(\frac{m}{M}\right)} \times 100\% = \frac{\left(\frac{S_{cv}}{vzF}\right)}{\left(\frac{m}{M}\right)} \times 100\%$$

Where S_{cv} is the integrated area of the Co(II)/Co(I) redox peak from CV, v is the scan rate, z is the electron transfer number of Co(II)/Co(I) (Z=1 in this case), F is the Faraday constant (96485 C mol^{-1}), m is the total mass of CoPc on the electrode, and M is the molar mass of CoPc (571.46 g mol^{-1}).

Long-term electrolysis was performed in a modified setup, where an external electrolyte reservoir was connected to the cathodic chamber via a circulation pump. 10 mL of electrolyte was maintained in the cathodic chamber, while 200 mL was stored in the external reservoir (100 mM Na_2SO_4, 25 mM Na_2SO_3). Continuous CO_2 bubbling was supplied at a flow rate of 20 mL min^{-1} throughout the electrolysis. The configuration is displayed in Figure S25.

Product quantification

Gaseous products were quantified using a Gas chromatography (GC) equipped with a thermal conductivity detector and a flame ionization detector. Argon (99.99%) was used as the carrier gas. The proton nuclear magnetic resonance (^1H NMR) spectroscopy was used to detect liquid products. A typical NMR sample preparation was performed as follows: 0.4 mL of electrolyte was mixed with 0.1 mL of D_2O, and then 0.1 mL 5 mM of DMSO aqueous solution was added as an internal standard.

Calculation of product Faraday efficiency and partial current density

Calculation of FE: the FE calculation method used for the reduction product is based on the equation below:

$$FE = \frac{c \times V \times n \times F}{Q} \times 100\%$$

Where c is the product concentration (e.g. mol L^{-1} for liquid products), V is the electrolyte volume (L), n is the number of transferred electrons to generate the product (n=2 for $HCOO^-$, CO, and H_2, n=4 for HMS, n=6 for MeOH), F is the Faraday constant (96485 C mol^{-1}), and Q is the total charge (C)

Calculation of partial current density: The partial current density of a specific product is calculated as shown below:

$$Partial\ current\ density = J \times FE_{product}$$

Where J is the total current density (mA cm^{-2}) obtained from LSV data.

The error bars correspond to the standard deviation from three independent measurements.

Computational details

DFT calculation: All calculations were carried out using Gaussian 16.[1] Geometries were optimized at the M06-L functionals.[2] The Stuttgart-Dresden (SSD) basis set was employed for Co, Ni, and Cu atoms,[3, 4] while the 6-31g(d) basis set was used for all other elements.[5] The interaction energies were then refined by M06-L/def2TZVP-SMD[6] single-point energy calculations in water solution using the SMD solvation model.[7] The IGM analysis was performed using the Multiwfn 3.8.[8]

***Ab initio* molecular dynamics (AIMD)**: The dynamic behavior of the adsorbed $*CH_2O$ intermediate on the CoPc surface was investigated via AIMD simulation using the ORCA 6.0.1 package.[9, 10] The simulations were performed at the B98-3c level of theory,[11] which provides an efficient and accurate description of both dispersion and basis-set superposition effects for large systems. The temperature was set at 298.15 K. The total simulation time was 2 ps, and the trajectory was sampled every 0.5 fs to monitor the structural fluctuations of the HCHO on the surface of CoPc.

AIMD simulations of cation effect on the hydrogen distribution around *CO and $*CO_2$ were performed using the CP2K code.[12] First, the structures of the *CO and $*CO_2$ intermediates adsorbed on a carbon nanotube were optimized. A graphene layer was placed at the bottom of a simulation box with dimensions of 19.6 x 17.0 x 15.0 Å^3, and the *CO and $*CO_2$ intermediates were positioned above the graphene surface. Geometry optimizations were carried out using the PBE functional. The DZVP-GTH-PBE basis set was applied for C, H, O, and N atoms, while DZVP-MOLOPT-SR-GTH was used for Co.[13, 14] Dispersion interactions were corrected using the DFT-D3 scheme.[15] For the subsequent AIMD simulations, the optimized atomic coordinates were kept fixed. A single Cs^+ ion and 145 water molecules were then added into the simulation box, and the system was modeled using the GFN1-xTB method.[16] Periodic boundary conditions were applied in the XY plane. The simulation temperature was set to 298 K. The system was first equilibrated for 1 ps under the NPT ensemble, followed by a 10 ps production run under the NVT ensemble, with snapshots recorded every 10 fs. The radial distribution function (RDF) of H atoms around the $^*CO$ and $^*CO_2$ was subsequently analyzed using VMD 1.9.3.[17]

Specific energy consumption of HMS (kWh kg^{-1}):

$$\mathrm{SEC}=\frac{E_{mol}}{M_{HMS^-}}=\frac{U_{cell}\cdot Q_{mol}}{M_{HMS^-}}=\frac{U_{cell}\cdot\frac{nF}{FE_{HMS}}}{M_{HMS^-}}=\frac{2.5\ \mathrm{x}\ \frac{4\ \mathrm{x}\ 96485}{0.257}}{111.09}=33794\ \mathrm{J\ g^{-1}}=9.4\ \mathrm{kWh\ kg^{-1}}$$

Cathodic potential: $E=-1.25V_{RHE}$; Assumed full-cell voltage: $U_{cell}\approx 2.5V$; $FE_{HMS}=0.257$; n=4; F=96485 C mol^{-1}; 1kWh=3600000 J.

Separation and purification of products

100 mL of the electrolyte collected after 5 h of electrolysis was adjusted to a mildly acidic environment by adding 1 mL of 1 M H_2SO_4 to stabilize HMS. The solution was then dried using a rotary evaporator at 60°C. During evaporation, MeOH vapor condensed and was collected in the receiving flask. Meanwhile, HMS together with the electrolytes Na_2SO_4 and Na_2SO_3 remained as solids in the evaporation flask. The resulting solid was dispersed in a mixed solvent of ethanol and water (9:1 v/v). This is primarily because organic compound (e.g. HMS) is significantly more soluble in ethanol than inorganic salts (e.g. Na_2SO_4 and Na_2SO_3). As a result, most inorganic salts precipitated as solids while HMS dissolved in the liquid phase. Filtration removed the residual inorganic salts, which were subsequently dried in air at 70°C for 3 h to obtain highly pure Na_2SO_4. The filtrate was then concentrated again by rotary evaporation to afford solid HMS powder, and the ethanol-water solvent mixture was recovered for reuse. ^1H NMR spectroscopy of the obtained HMS solid displayed only the characteristic resonances of HMS, and gravimetric analysis indicated a purity higher than 87%.

Calculation of atom economy and FE-adjusted E-factor:

1. Overall stoichiometry for HMS formation

A charge-balanced overall reaction for forming HMS^- can be written as:

$CO_2 + SO_3^{2-} + 5H^+ + 4e^- \rightarrow HOCH_2SO_3^- + H_2O$ (Equation S1)

2. Atom economy

The molar mass of HMS^- ($HOCH_2SO_3^-$) is: 111.09 g mol^{-1}

The only stoichiometric byproduct in Eq. (S1) is water (M_{H_2O} = 18.02 g mol^{-1})

Therefor, the atom economy is:

$$\text{Atom economy} = \frac{M_{HMS-}}{M_{HMS-} + M_{H2O}} = \frac{111.09}{111.09 + 18.02} = 0.860\ (86.0\%)$$

3. FE-adjusted E-factor

To quantify waste generation associated with non-target charge consumption, an FE-adjusted E-factor is calculated using the experimentally measured product distribution (HMS/CO/MeOH/H_2). Electron stoichiometries were taken as: HMS (4 e^- mol^{-1}), CO (2e^- mol^{-1}), MeOH (6e^- mol^{-1}), and H_2 (2e^- mol^{-1}).

For a basis of producing 1 mol HMS^-, the total moles of electrons passed are:

$$n_{e,total} = \frac{n_{e-,HMS}}{FE_{HMS}} = \frac{4}{0.257} = 15.564\ mol\ e^{-1}$$

Electrons allocated to each coproduct i are:

$$n_{e,i} = FE_i \times n_{e,total}$$

and the corresponding moles of coproduct are:

$$n_i = \frac{n_{e,i}}{v_i}$$

where v_i is the electron number per mole of product *i* (CO:2, MeOH:6, H_2: 2).

Using $FE_{CO} = 0.224$, $FE_{MeOH} = 0.369$, $FE_{H2} = 0.076$:

$$n_{CO} = \frac{0.224 \times 15.564}{2} = 1.743$$

$$n_{MeOH} = \frac{0.369 \times 15.564}{6} = 0.957$$

$$n_{H2} = \frac{0.076 \times 15.564}{2} = 0.591$$

Masses of co-products (using $M_{CO} = 28.01$, $M_{MeOH} = 32.04$, $M^{H2} = 2.02$ g mol^{-1})

$$m_{byproducts} = n_{CO}M_{CO} + n_{MeOH}M_{MeOH} + n_{H2}M_{H2} = 80.64g$$

Thus, the FE-adjusted E-factor is:

$$E_{FE} = \frac{m_{byproducts}}{M_{HMS^-}} = \frac{80.64}{111.09} = 0.73\ kg\ kg^{-1}$$

Table S1. Comparison of electrocatalytic C-S coupling reaction conditions and performances.

Electrocatalysts	**Products**	**FE (%)**	**Partial Current density (mA cm^{-2})$^{\#}$**	**Stability (h)**	**Condition**	**Refs.**
CoPc/CNT	HMS	25.7	-4.9	>5	H-cell, 0.1 M Na2SO4 and 0.025 M Na_2SO_3	This work
Cu	HMS, SA and MS	6.8 (three C-S products)	-2.1	-	1 M KOH and 0.2 M Na_2SO_3	*Nat. Synth.* **2023,** *2* (8), 757-765.
Cu-BDC-XN	MS	13.77	≈-2	-	H-cell, 1 M KOH and 0.2 M Na_2SO_3	*Angew Chem. Int. Ed.* **2025**, e202509851
CoPc-NH_2/CNTs	HMS	~12	18	FE decreased to ~8% after 5 h	flow electrolyser, 0.3 M $KHCO_3$ + 0.4 M Na_2SO_3	*Nat. Synth.* **2026,** 10.1038/s44160-025-00961-x

#: Current density at the potential with the highest FE

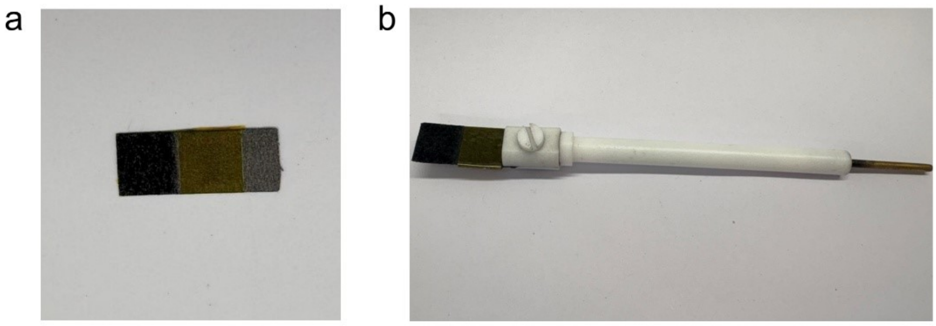

Figure S1. Photographs of (a) electrode and (b) and electrode attached to the holder to give the configuration used in this study.

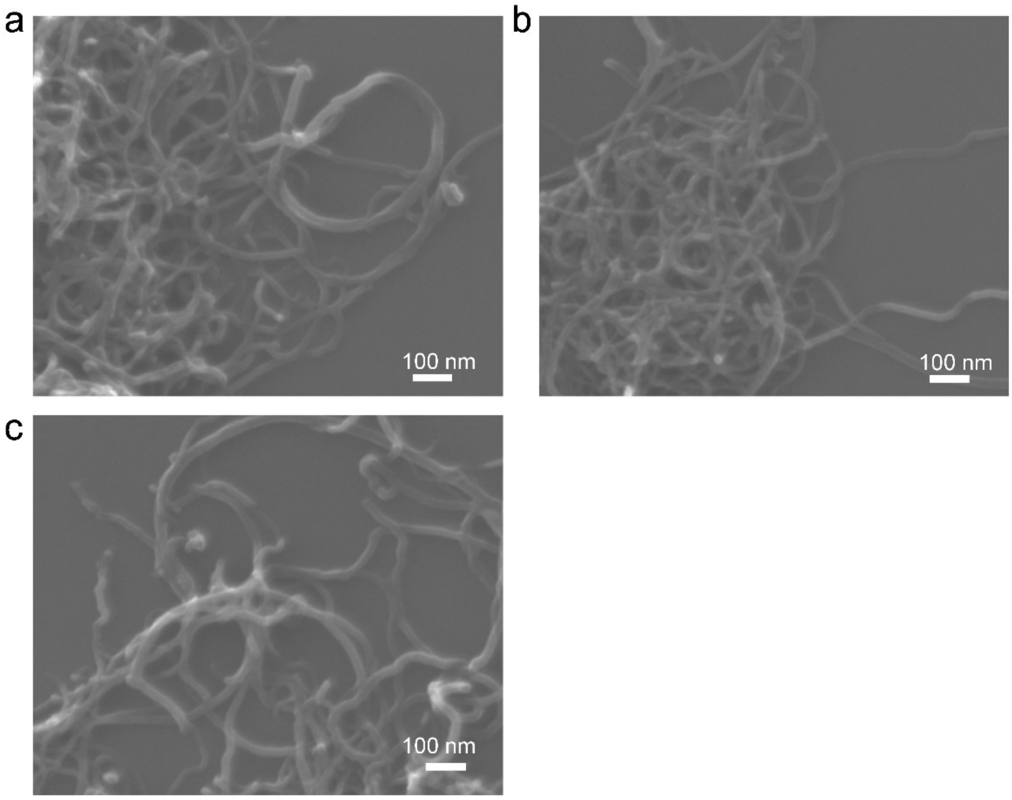

Figure S2 SEM images of (a) CoPc/CNT, (b) NiPc/CNT and (c) CuPc/CNT.

Only the morphology of the CNTs was observed in the SEM image, and no distinct nanocrystals were detected, indicating that all MPc molecules were adsorbed onto the CNT surface.

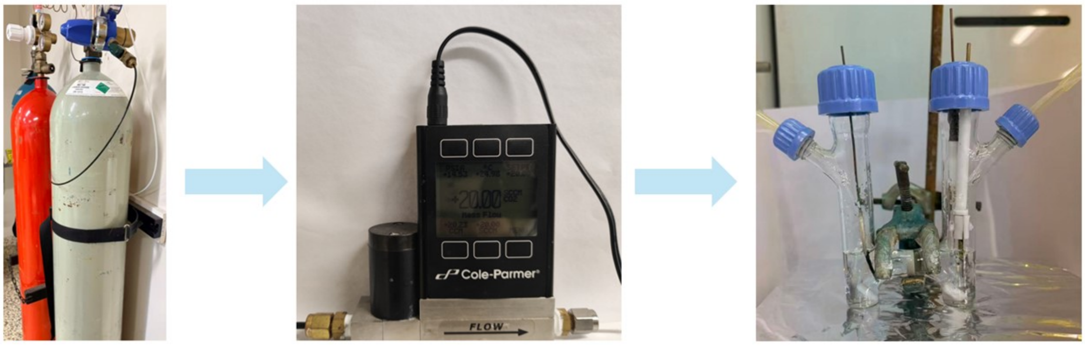

CO_2 cylinder CO_2 flowmeter H-type cell

Figure S3. Photographs of the CO_2 supply system which includes a gas cylinder and flow controller, and the electrochemical cell used in this study.

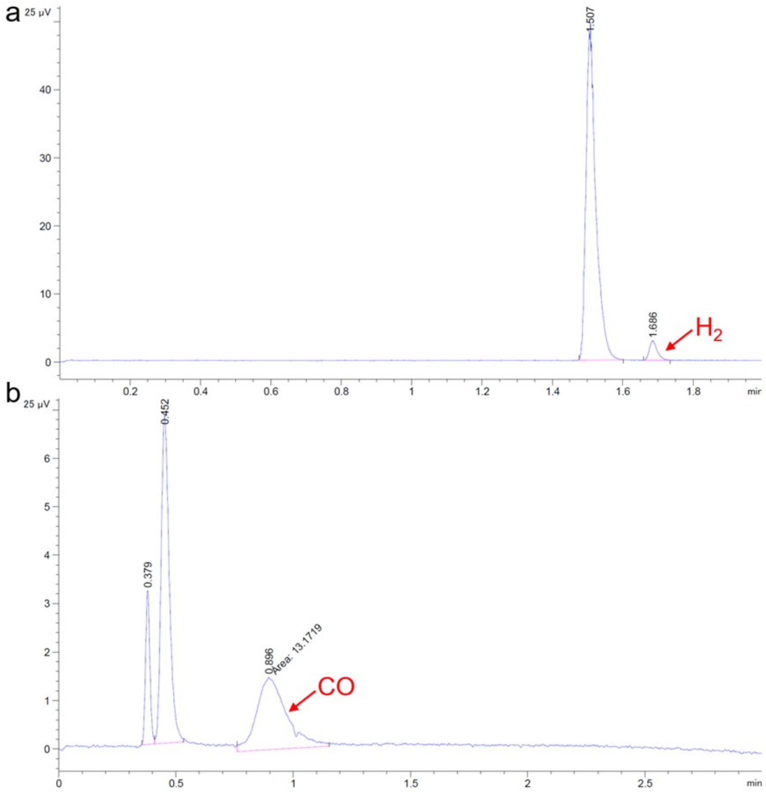

Figure S4. GC data obtained for (a) H_2 and (b) CO during C-S coupling reduction process.

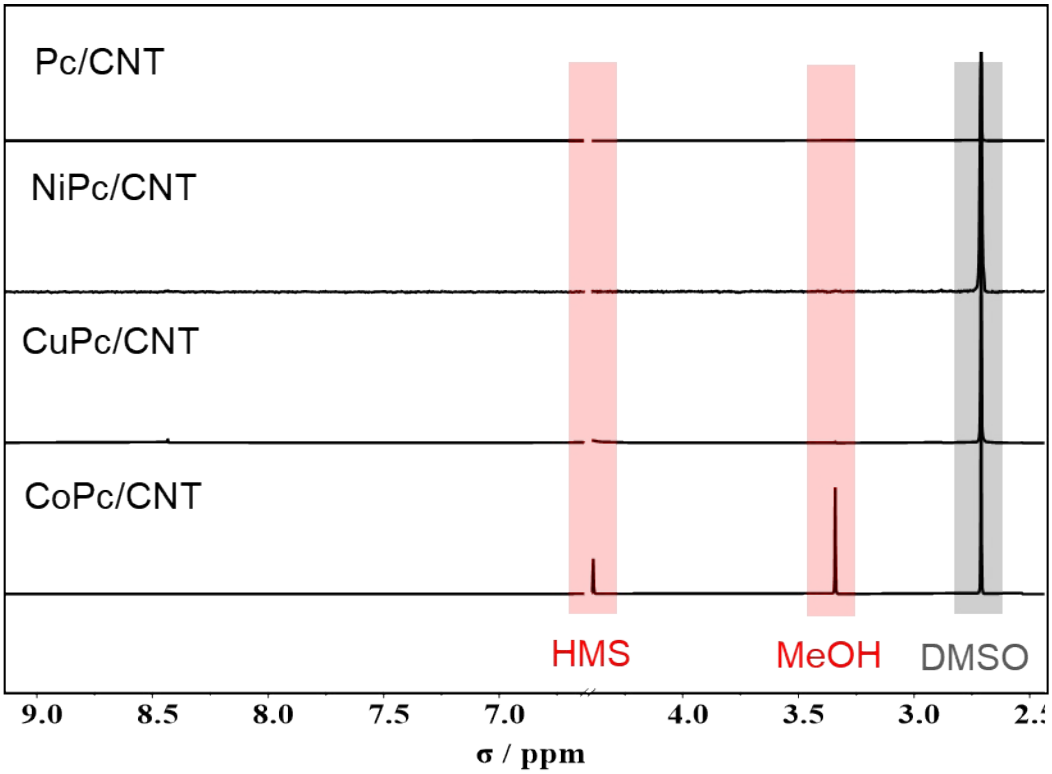

Figure S5. ^{1}H NMR spectra obtained after electrolysis at E = -1.25 V_{RHE} for 30 min using CoPc/CNT, CuPc/CNT, NiPc/CNT, and Pc/CNT as the catalyst in a CO_2-saturated solution containing 100 mM Na_2SO_4 and 50 mM Na_2SO_3.

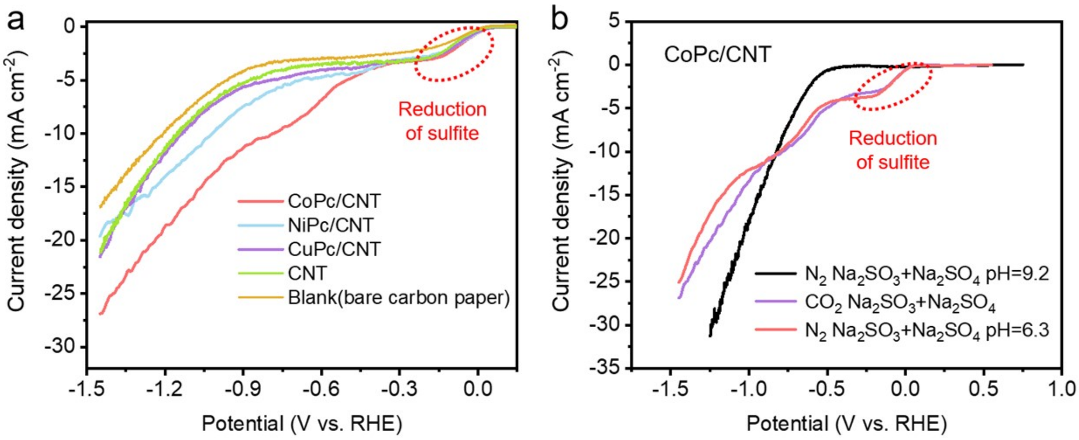

Figure S6. (a) LSV data of the blank (bare carbon paper), and carbon paper modified with CNT, CoPc/CNT, CuPc/CNT or NiPc/CNT in a CO_2-saturated solution containing 100 mM Na_2SO_4 and 50 mM Na_2SO_3. (b) LSV data of CoPc/CNT in a CO_2-saturated solution (pH=6.3), a N_2-saturated solution (pH=9.2), or an acidified N_2-saturated solution (pH of 6.3, adjusted using H_2SO4), all containing 100 mM Na_2SO_4 and 50 mM Na_2SO_3.

Under a CO_2 atmosphere (pH = 6.3), a reduction process was observed around -0.1 V_{RHE} in the presence and absence of MPc/CNT on the carbon paper, which was not observed under a N_2 atmosphere (pH = 9.2). This process is likely associated with the reduction of sulfite species on the carbon paper in this weakly acidic medium,[18, 19] where protonated sulfite is more prone to reduction, as confirmed by the voltammogram obtained in an acidified N_2-saturated electrolyte solution (pH = 6.3). Since the magnitude of the plateau current is far below the mass transport-limiting current, this process is likely under kinetic control.

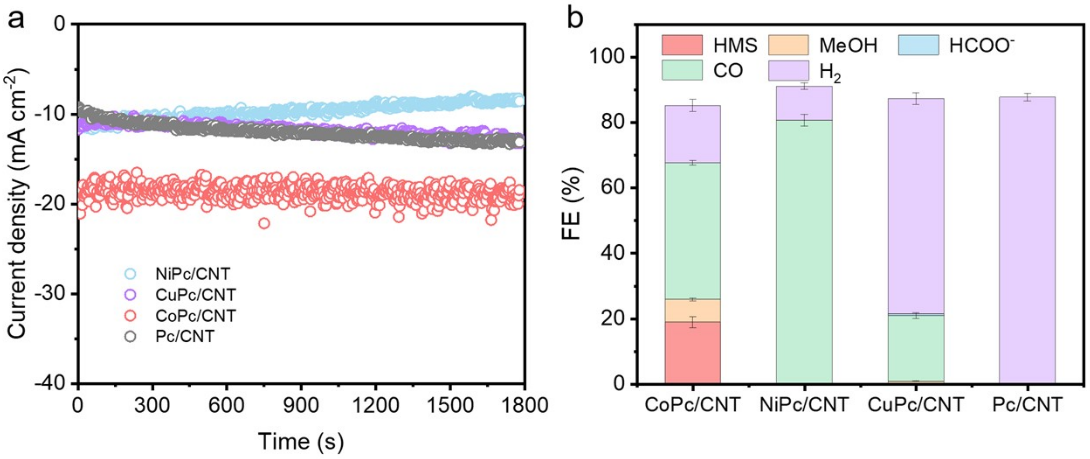

Figure S7. (a) The i-t data and (b) FEs of CoPc/CNT, CuPc/CNT, NiPc/CNT and Pc/CNT in a CO_2-saturated solution containing 100 mM Na_2SO_4 and 50 mM Na_2SO_3.

Comparative analysis of the FE for HMS in (b) obtained using different catalysts reveals that Co serves as the active site in the electrocatalytic C-S coupling system.

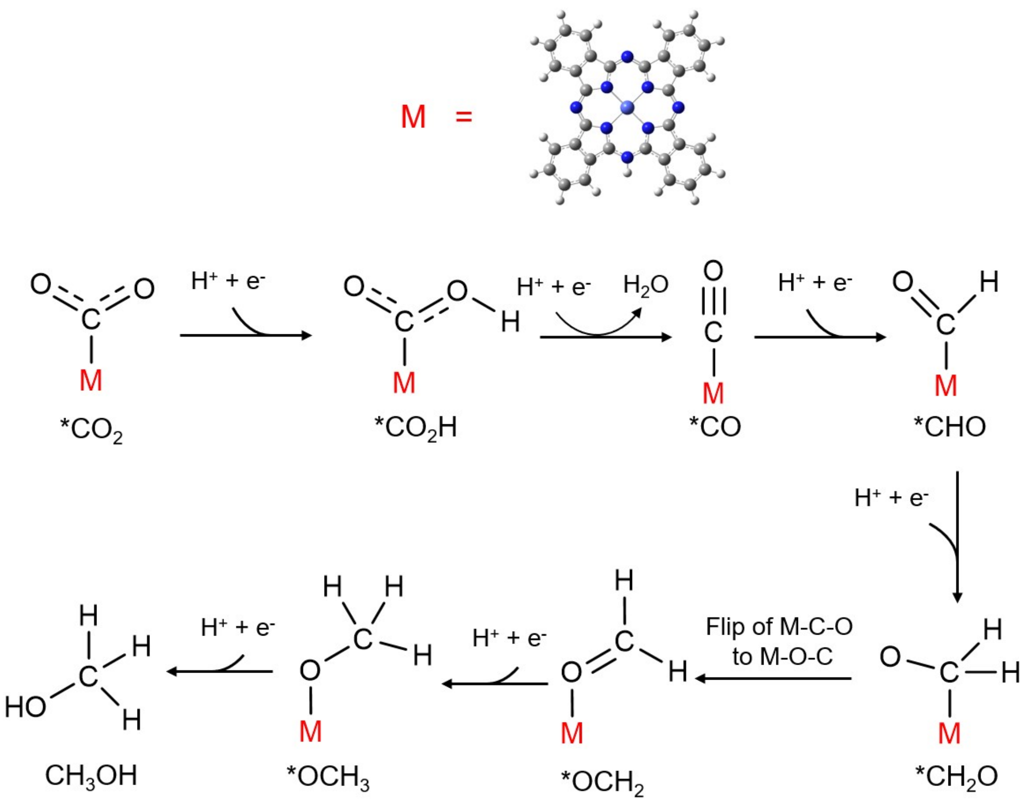

Figure S8. The eCO_2RR pathway.

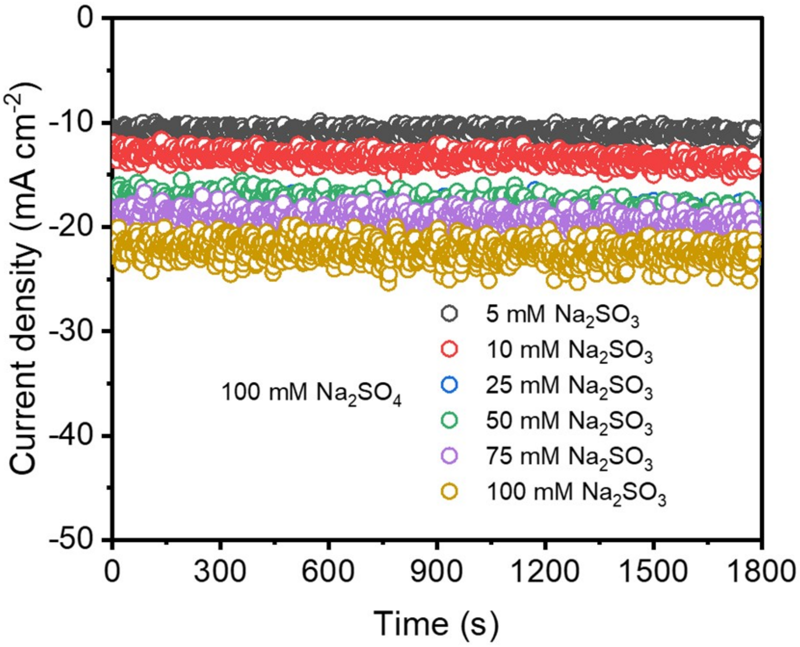

Figure S9. The i-t data of CoPc/CNT in a CO_2-saturated solution containing 100 mM Na_2SO_4 and different Na_2SO_3 concentration.

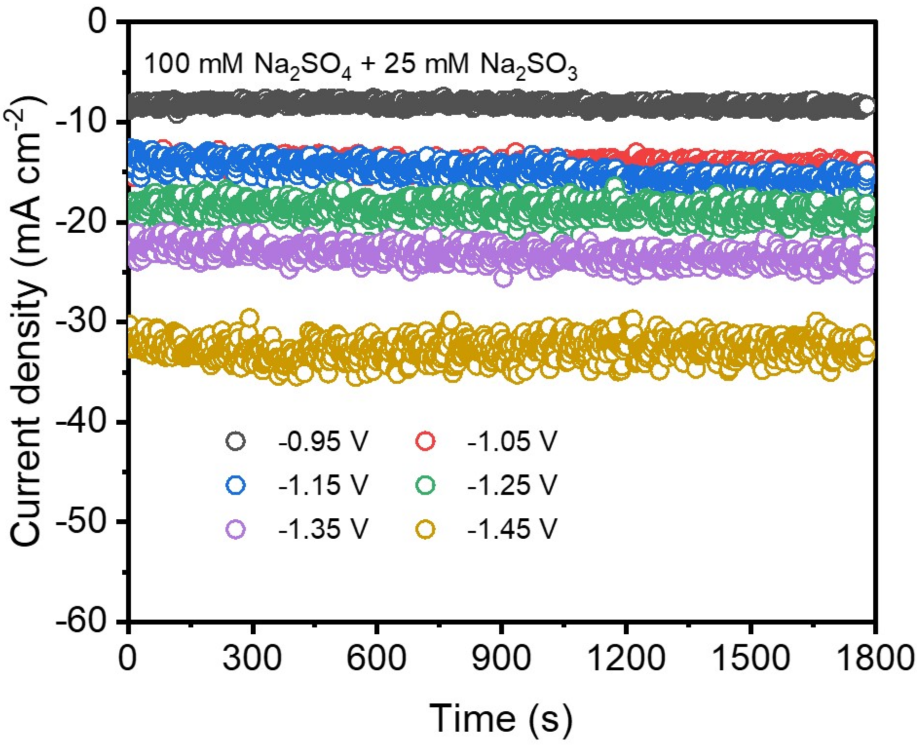

Figure S10. The i-t data using CoPc/CNT as the catalyst in a CO_2-saturated solution containing 100 mM Na_2SO_4 and 25 mM Na_2SO_3.

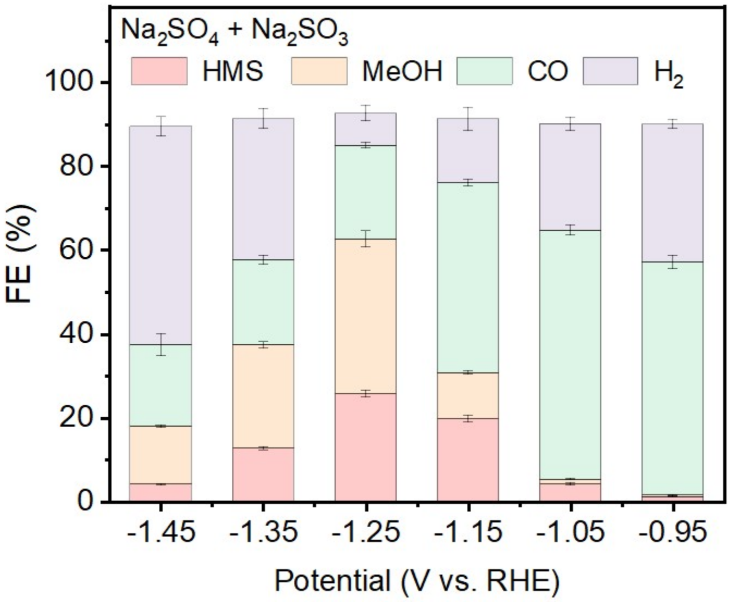

Figure S11. FEs using CoPc/CNT as the catalyst in a CO_2-saturated solution containing 100 mM Na_2SO_4 and 25 mM Na_2SO_3. Owing to the reduction of sulfite species, as shown in Figure S2, the overall FEs of the quantified products presented in this figure are less than 100%.

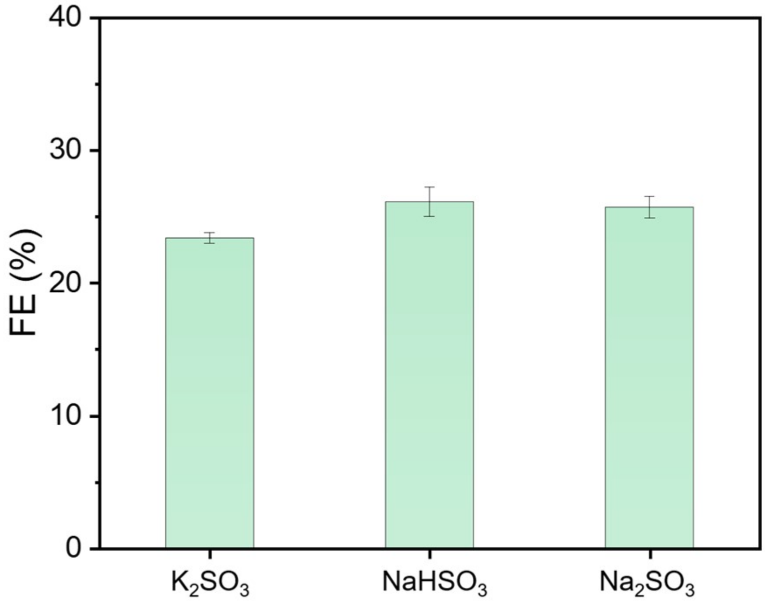

Figure S12. Comparison of FE values obtained by electrolysis at E=-1.25V_{RHE} in CO_2-saturated 100 mM Na_2SO_4 electrolyte containing 25 mM K_2SO_3, $NaHSO_3$, or Na_2SO_3. The error bars correspond to the standard deviation from independent measurements.

We evaluated the generality of our system by testing additional sulfur sources under identical conditions. Specifically, electrolysis was conducted in 100 mM Na_2SO_4 electrolyte containing 25 mM K_2SO_3, 25 mM $NaHSO_3$, or 25 mM Na_2SO_3, respectively, and the formation of HMS was quantified. At E = -1.25 V_{RHE}, the FE toward HMS were similar for different sulfur sources: 23.4 ± 0.4% for K_2SO_3, 26.1 ± 1.1 % for $NaHSO_3$, and 25.7 ± 0.8% for Na_2SO_3. These results indicate that the choice of sulfite/bisulfite precursor has minimal influence on the HMS selectivity under our reaction conditions, supporting the general applicability of the proposed C-S coupling strategy.

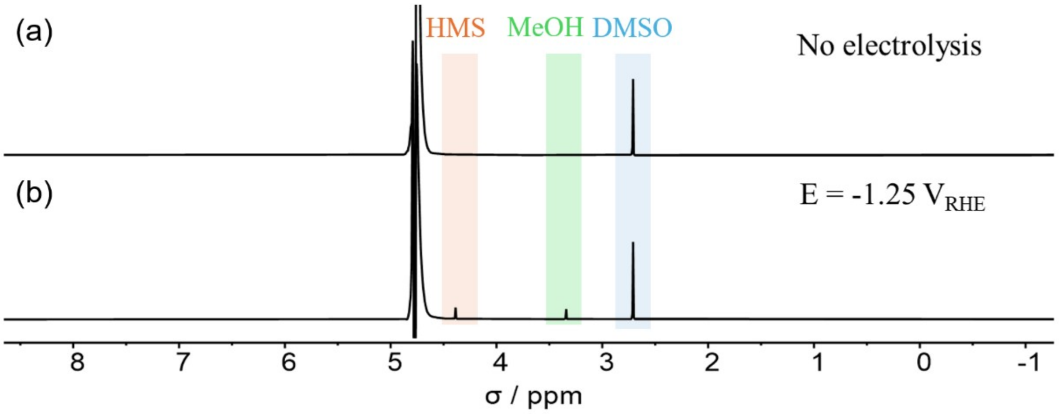

Figure S13. ^{1}H NMR analysis of the reaction using CO as the carbon source in 100 mM Na_2SO_4 electrolyte under (a) open-circuit conditions and (b) after 30 min of electrolysis ($E = -1.25\ V_{RHE}$). DMSO (5 mM) was used as the internal standard.

We conducted an alternative carbon source (CO) under otherwise identical conditions, both with and without electrolysis. In all cases, HMS formation was observed when CO was employed as the carbon source. These results indicate that C-S bond formation is not limited to CO_2 as the sole substrate model and further supports the broader applicability of the electrocatalytic C-S coupling strategy.

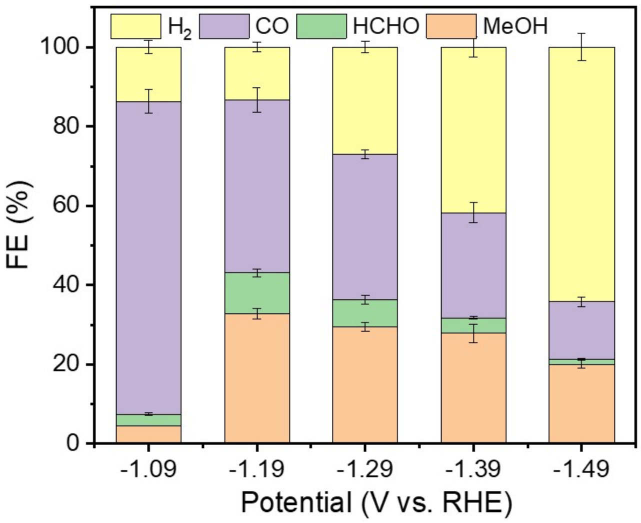

Figure S14. Electrocatalytic performance of a CoPc/CNT electrode in a CO_2-saturated solution containing 100 mM Na_2SO_4 as a function of applied potentials.

We conducted control electrolysis experiments in the absence of sulfite, using a CO_2-saturated solution containing 100 mM Na_2SO_4 as the supporting electrolyte. Under these conditions, the major CO_2 reduction products (CO, CH_3OH, and HCHO) were quantitatively analyzed (Figure S14). Notably, a measurable amount of formaldehyde was detected in the bulk electrolyte, indicating that this compound can indeed be generated and desorb into solution under the reaction conditions. This observation supports the feasibility of a desorbed-formaldehyde pathway.

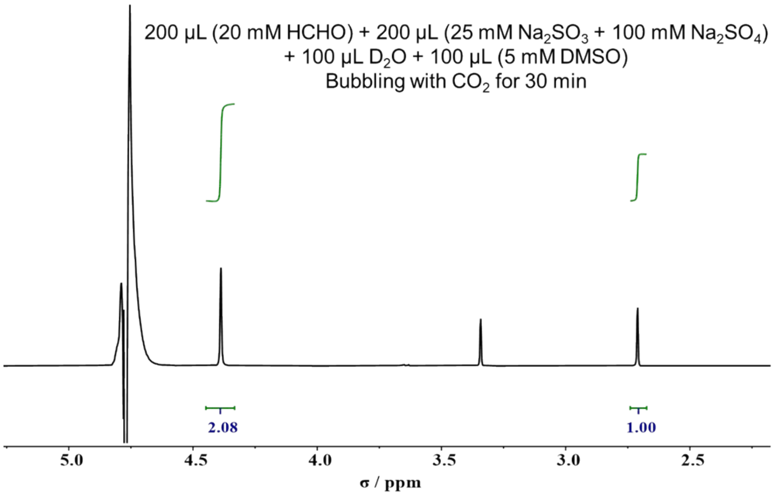

Figure S15. ^{1}H NMR data showing the formation of HMS from the reaction between HCHO and SO_3^{2-} under non-electrolytic conditions. The resonance at 2.71 ppm is due to DMSO, while that at 4.39 ppm is assigned to HMS.

Control experiments also were performed in which formaldehyde and sodium sulfite were directly mixed under non-electrolytic conditions. In this case, HMS formation was readily observed, demonstrating that sulfite effectively captures formaldehyde to form the C-S product. These results again support the key role of formaldehyde as a reactive intermediate in the C-S bond formation process.

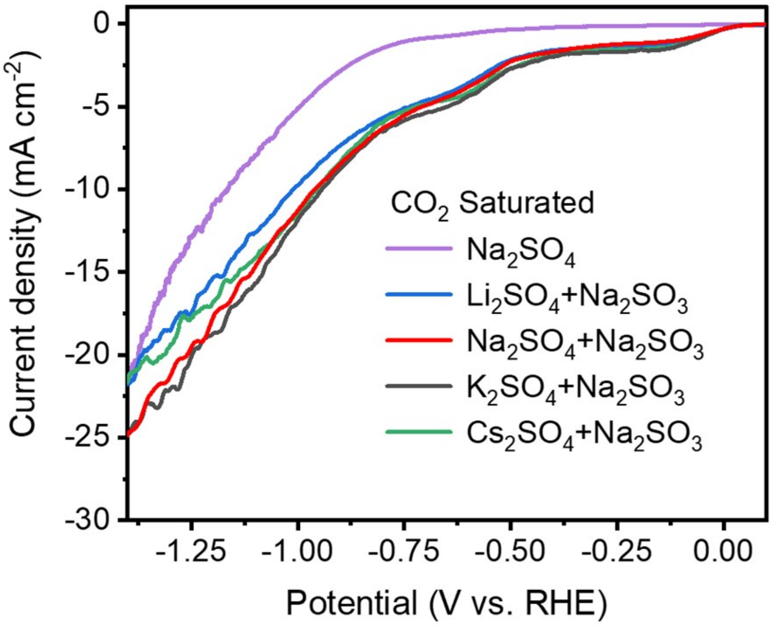

Figure S16. LSV data in a CO_2-saturated solution containing 100 mM alkali metal sulfate salts and 25 mM Na_2SO_3.

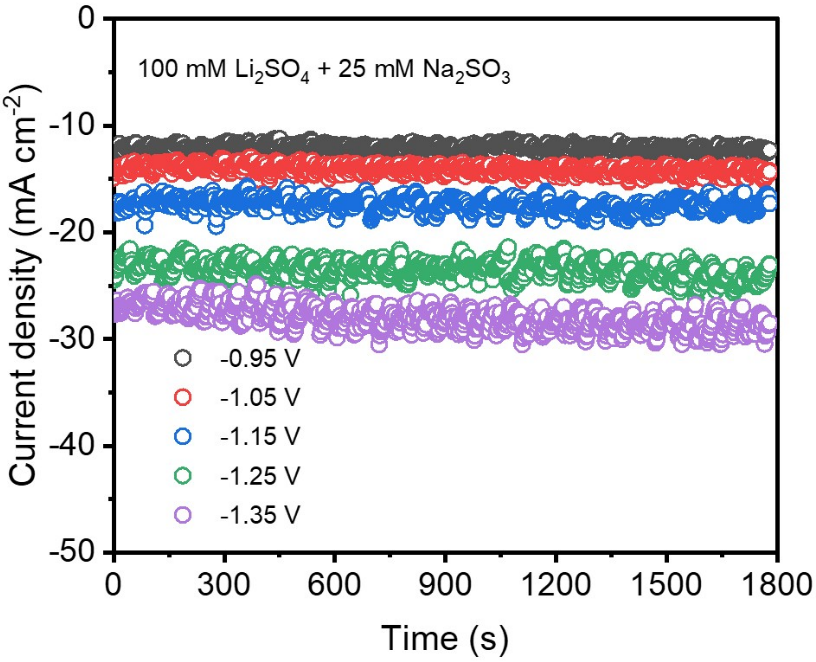

Figure S17. The i-t data in a CO_2-saturated solution containing 100 mM Li_2SO_4 and 25 mM Na_2SO_3.

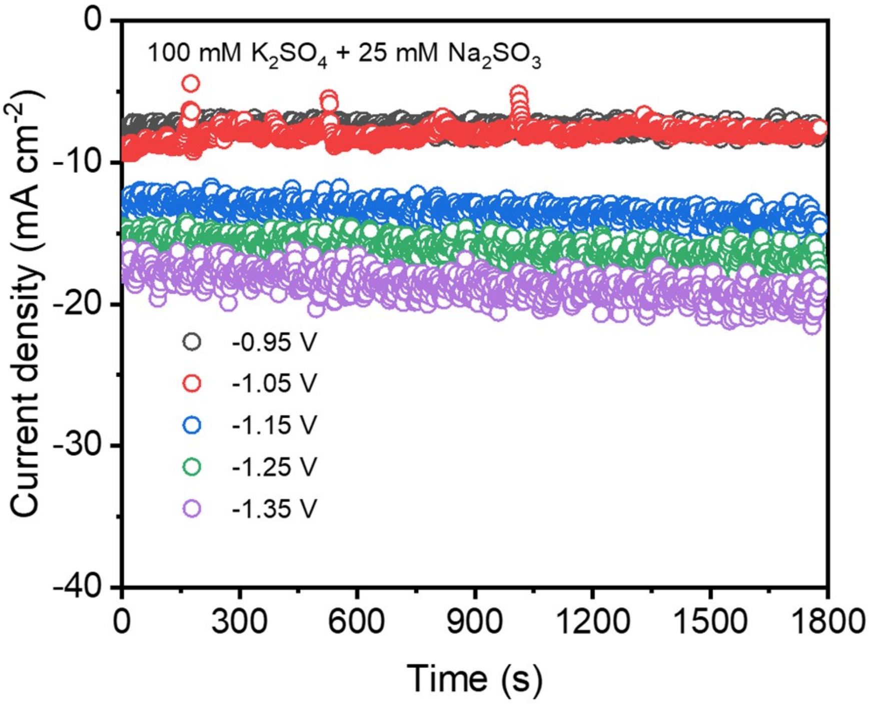

Figure S18. The i-t data in a CO_2-saturated solution containing 100 mM K_2SO_4 and 25 mM Na_2SO_3.

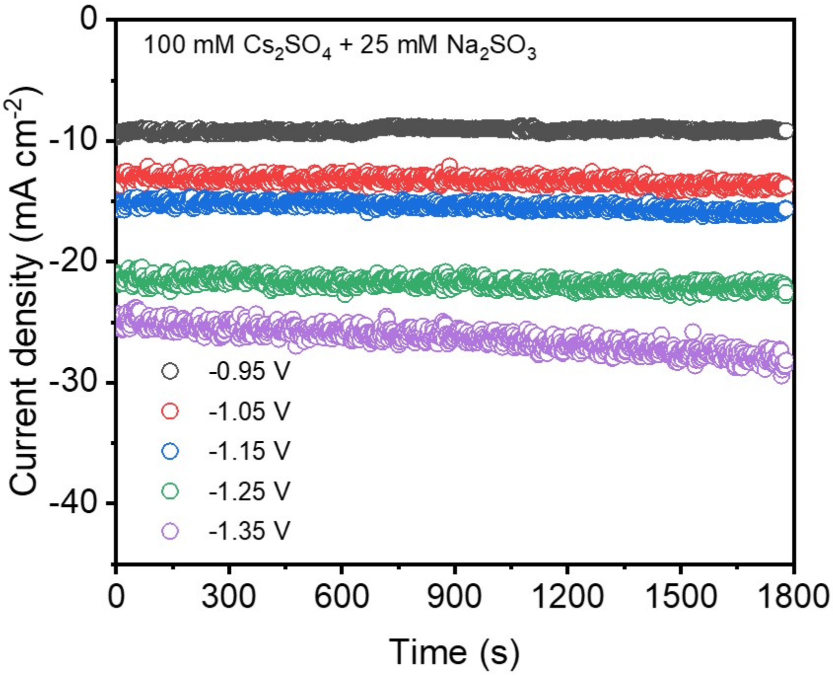

Figure S19.The i-t data in a CO_2-saturated solution containing 100 mM Cs_2SO_4 and 25 mM Na_2SO_3.

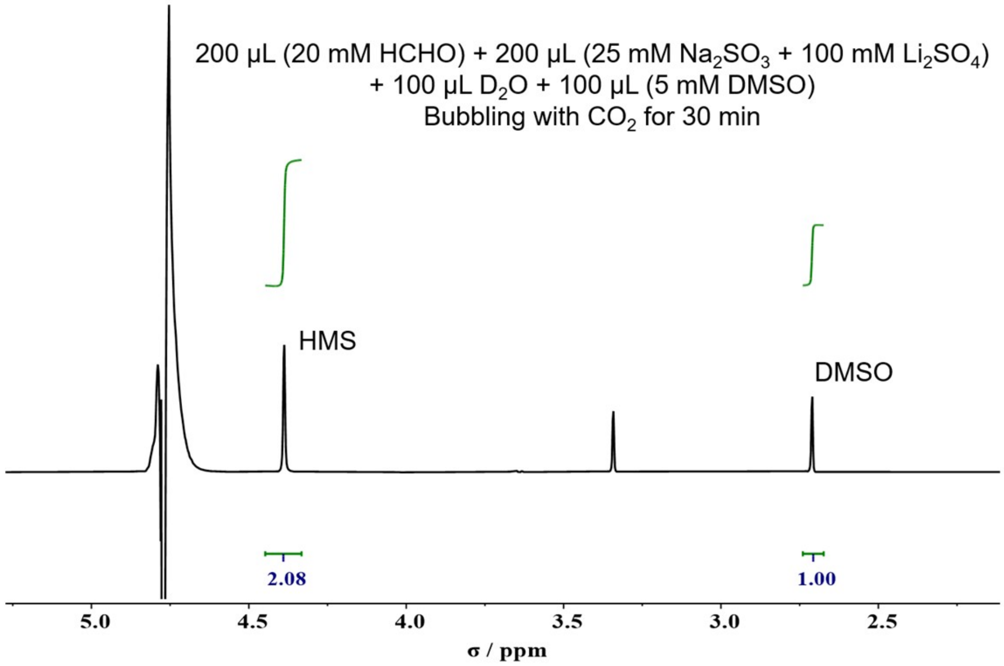

Figure S20. Effect of Li$^+$ on the formation of HMS from the reaction between HCHO and SO_3^{2-}. The peak at 2.71 ppm corresponds to DMSO, while the peak at 4.39 ppm is assigned to HMS.

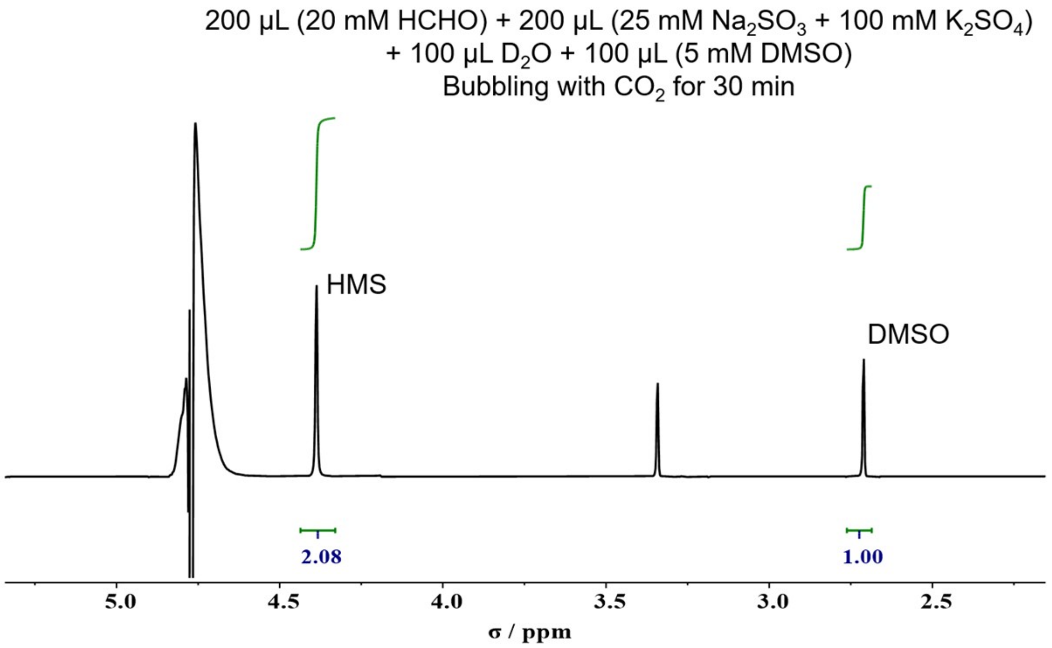

Figure S21. Effect of K^+ on the formation of HMS from the reaction between HCHO and SO_3^{2-}. The peak at 2.71 ppm corresponds to DMSO, while the peak at 4.39 ppm is assigned to HMS.

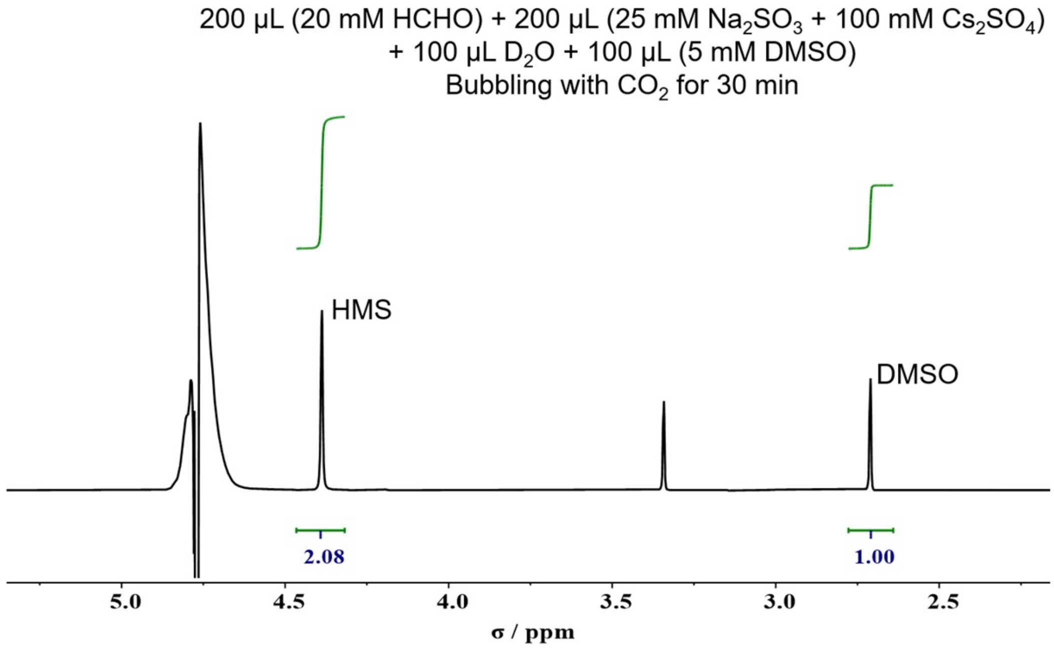

Figure S22. Effect of Cs$^+$ on the formation of HMS from the reaction between HCHO and SO$_3^{2-}$. The peak at 2.71 ppm corresponds to DMSO, while the peak at 4.39 ppm is assigned to HMS.

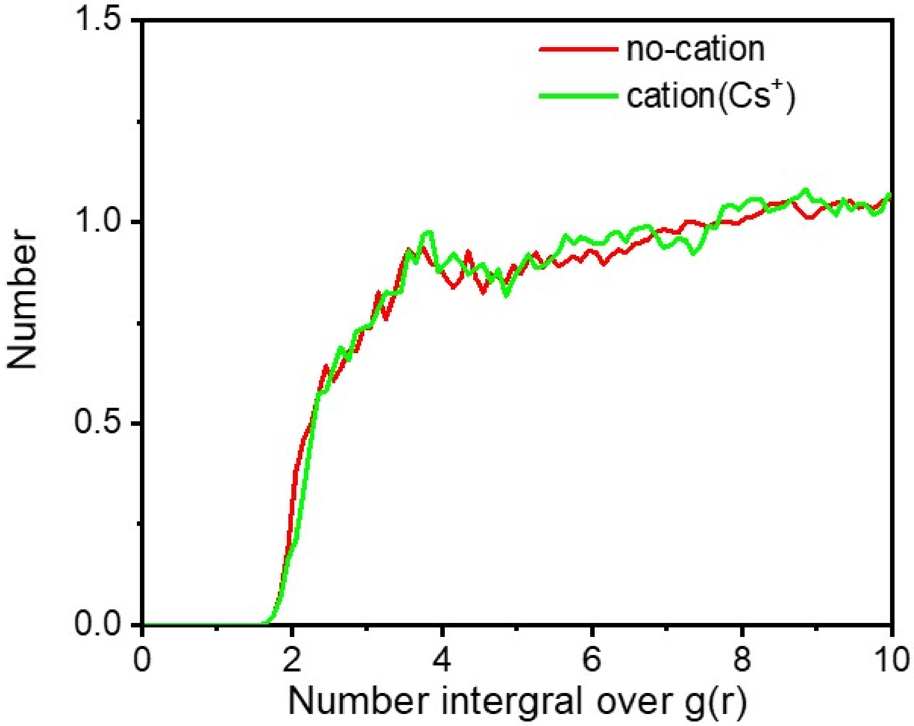

Figure S23. Analysis of radial distribution functions of hydrogen atoms in surrounding water molecules relative to the oxygen atom of $*CO_2$ in the absence and presence of Cs^+.

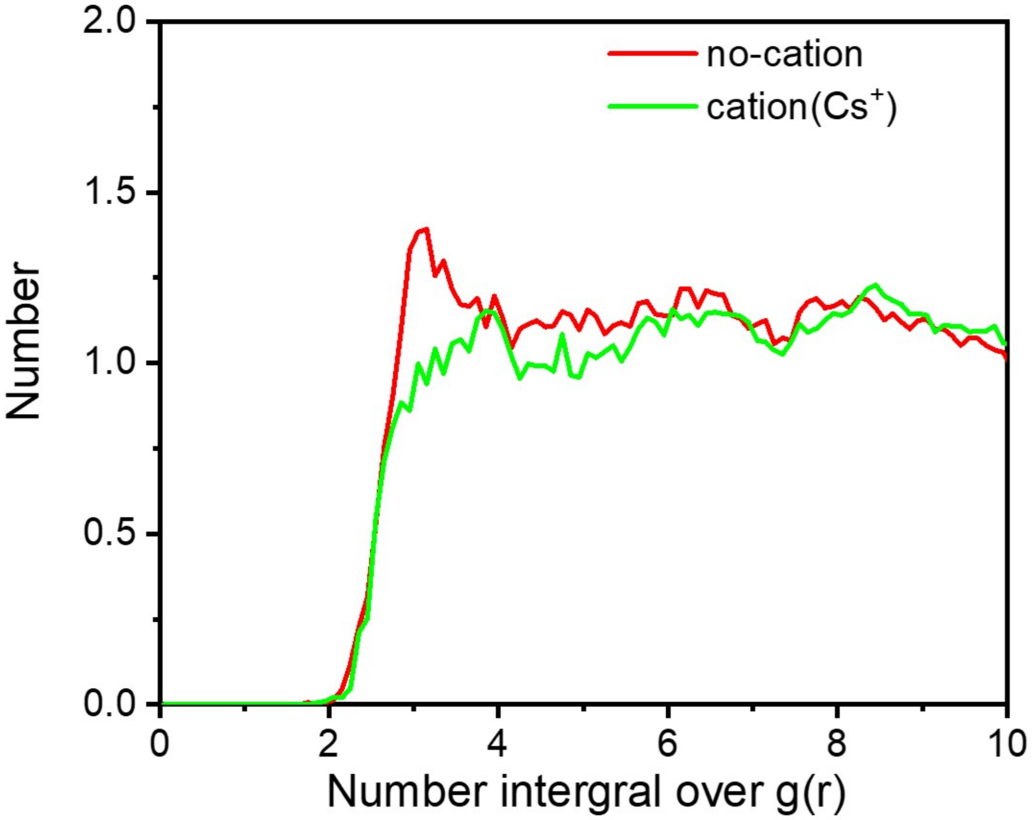

Figure S24. Analysis of radial distribution functions of hydrogen atoms in surrounding water molecules relative to the carbon atom of *CO in the absence and presence of Cs^+.

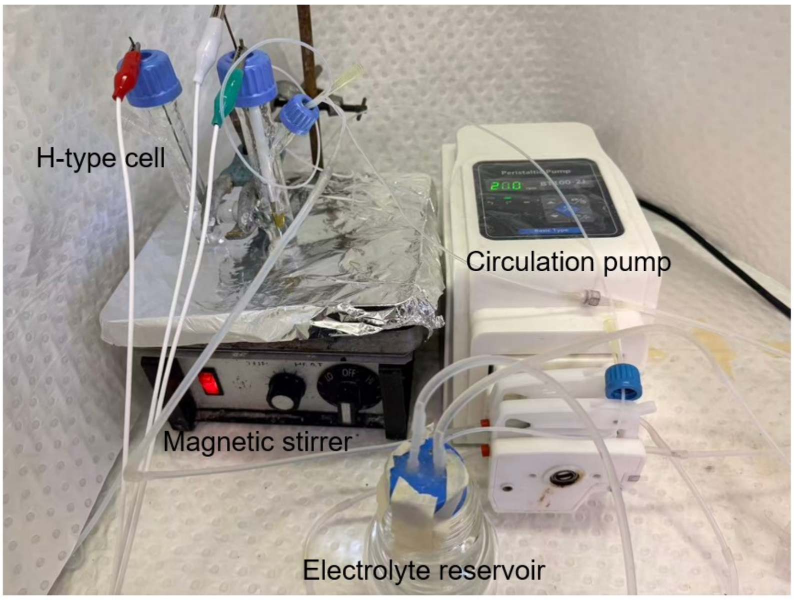

Figure S25. Photograph of the experimental configuration used for long term electrolysis.

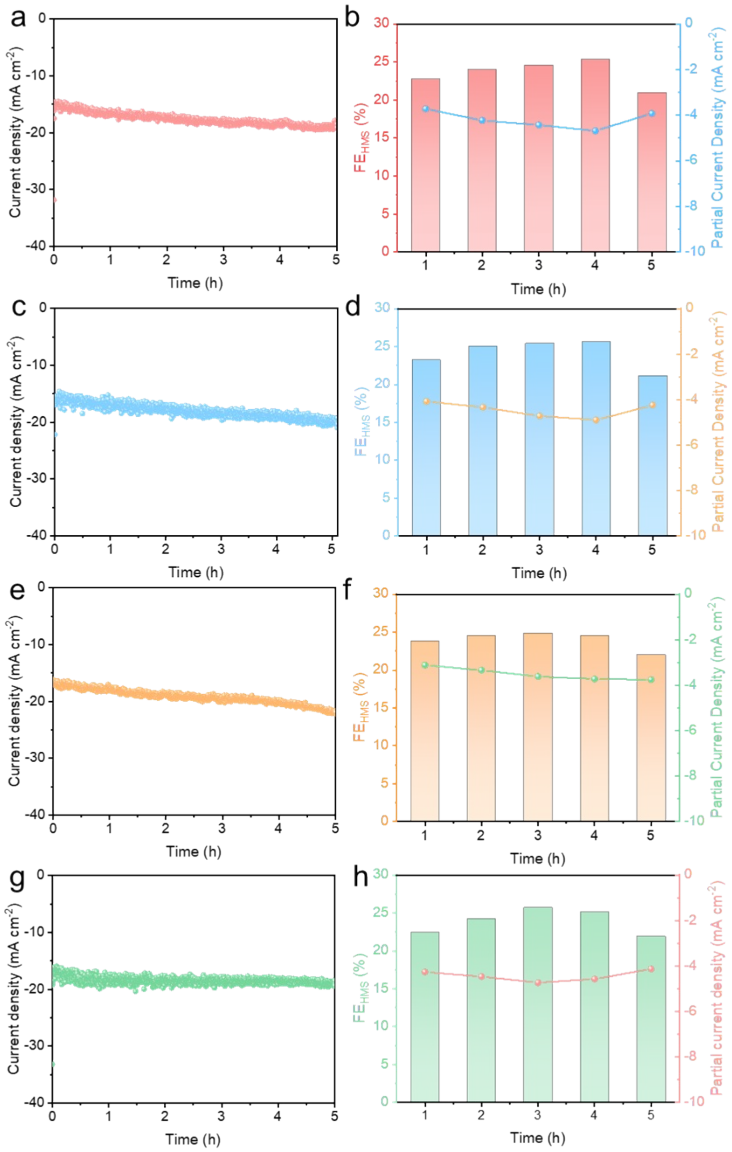

Figure S26. The i-t data (a, c, e and g) and the corresponding FE for HMS (b, d, f and h) over four consecutive 5h electrolysis cycles.

We performed four electrolysis cycles of CoPc/CNT under identical conditions to evaluate its stability and reusability. The corresponding FE and partial current density for HMS during the cycling tests are presented in Figure S26. The results show that after four cycles, both the FE and partial current density for HMS remain nearly unchanged, indicating that the CoPc/CNT catalyst maintains its electrocatalytic performance during the C-S coupling process and demonstrating its excellent cycling stability.

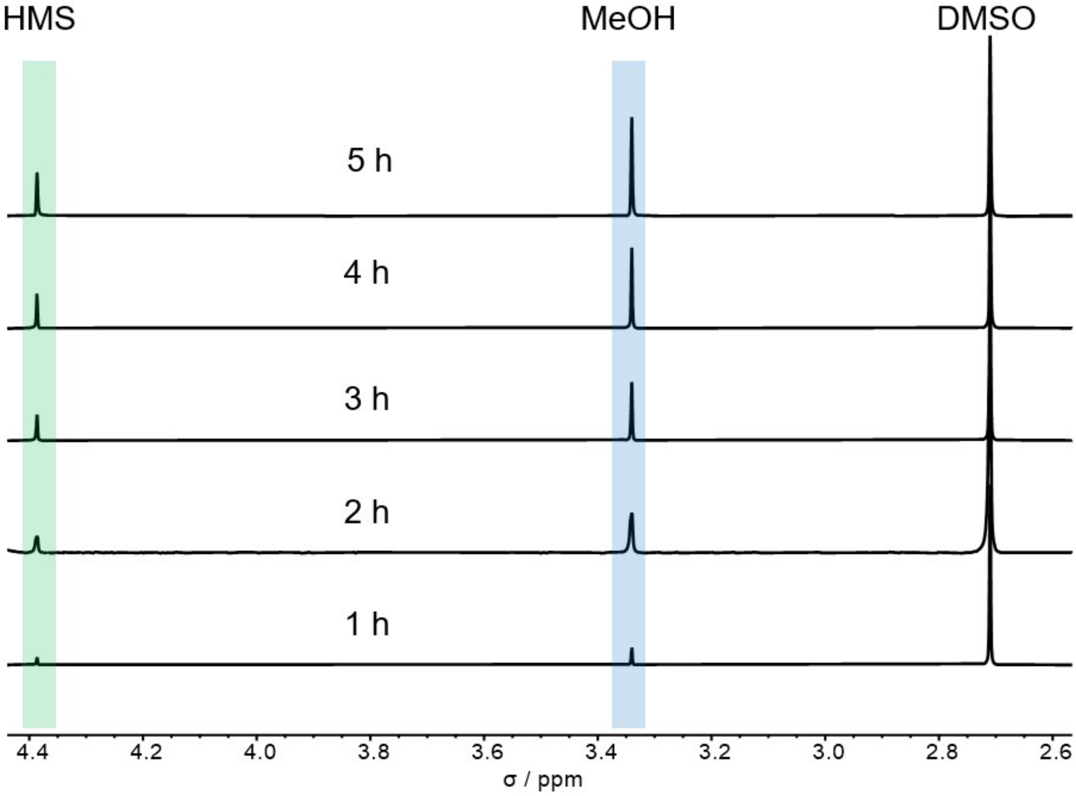

Figure S27. ^{1}H NMR spectra obtained after electrolysis 5 h at E = -1.25 V_{RHE} in a CO_2-saturated solution containing 100 mM Na_2SO_4 containing 25 mM Na_2SO_3 using CoPc/CNT as the catalyst.

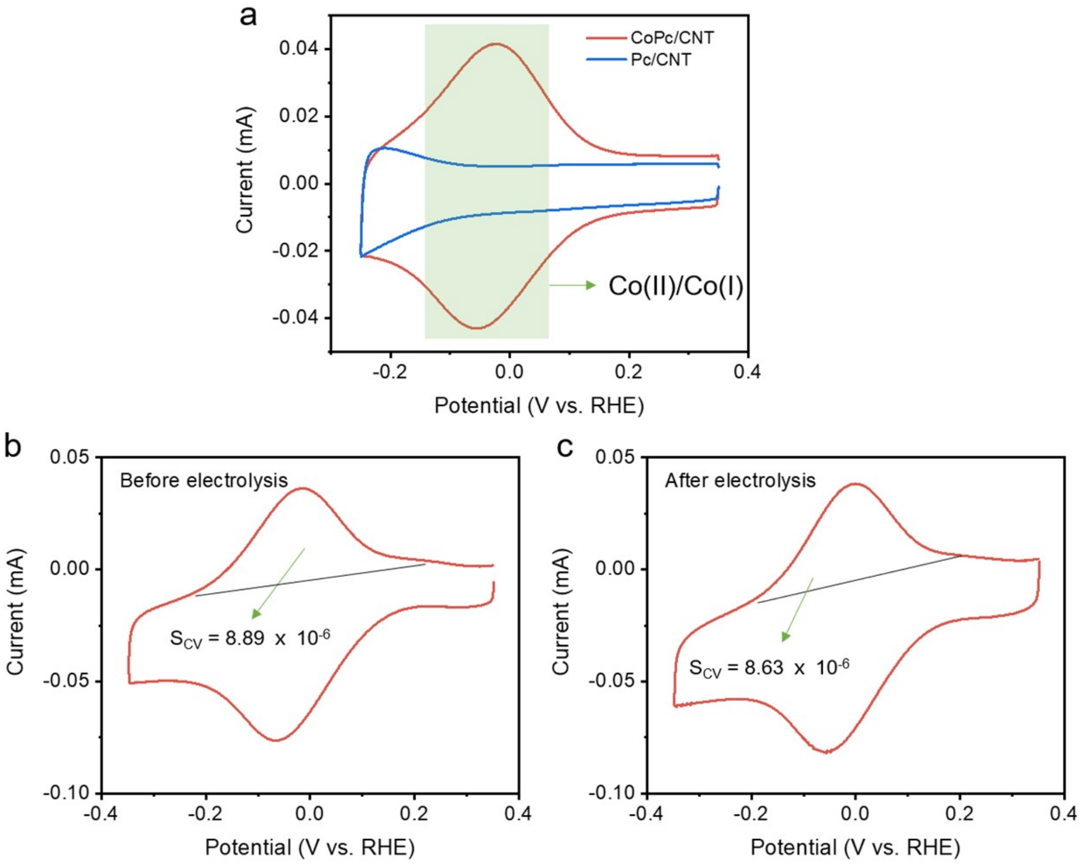

Figure S28. (a) CVs of the CoPc/CNT and Pc/CNT catalysts loaded on glass carbon electrodes in a N_2-saturated 100 mM Na_2SO_4 solution over the potential range of 0.35 V_{RHE} to -0.25 V_{RHE} at a scan rate of 0.1 V s^{-1}. (b, c) CVs of the CoPc/CNT catalyst (m_{CoPc} = 0.0006 mg) loaded on carbon paper in N_2-saturated 100 mM Na_2SO_4 over the potential range of 0.35 V_{RHE} to -0.34 V_{RHE} in at a scan rate of 0.1 V s^{-1} in a CO_2-saturated 100 mM Na_2SO_4 solution containing 25 mM Na_2SO_3 (b) before ($\eta_{before}\%$ = 87.7 %) and (c) after 5 h of electrolysis ($\eta_{after}\%$ = 85.1 %).

In (a), a well-defined redox process is observed around -0.05 V_{RHE} with the CoPc/CNT modified electrode but is absent with a Pc/CNT modified electrode, corresponding to the Co(II)/Co(I) redox transition. Since the optimal potential for the electrocatalytic C-S coupling reaction to produce HMS is approximately -1.25 V_{RHE} with CoPc/CNT, as shown in Figure S3b, the Co(0) state is likely responsible for the catalytic activity. This observation is consistent with previously reported results.[20]

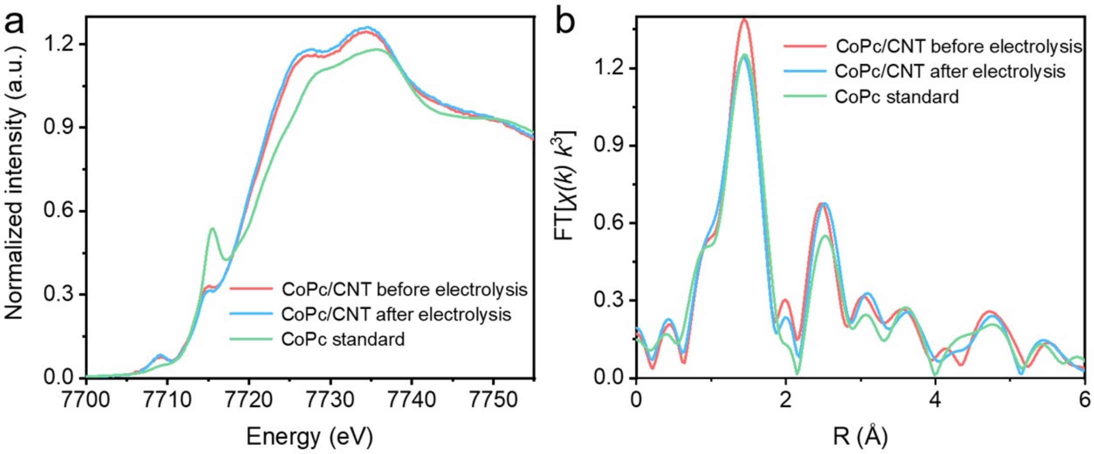

Figure S29. (a) Co K-edge XANES spectra. (b) EXAFS spectra of CoPc-CNT before and after electrolysis and CoPc reference.

Table S2. ICP-MS analysis of Co content in electrolyte before and after electrolysis on CoPc/CNT at E = -1.25 V_{RHE} for 5 h.

Sample	**Co concentration**
electrolyte before electrolysis	below the detection limit of 0.1 ppb
electrolyte after electrolysis	below the detection limit of 0.1 ppb

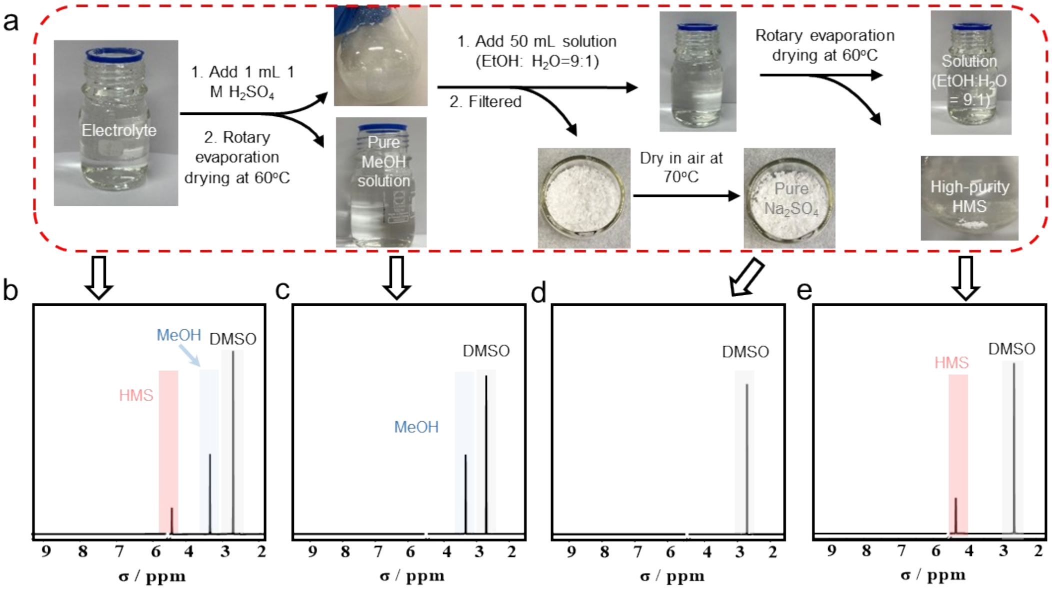

Figure S30. (a) Optical photographs of the purification process for MeOH, HMS, and Na_2SO_4. Partial ^{1}H NMR spectra of (b) the electrolyte after electrolysis, (c) the solution obtained after rotary evaporation, (d) the solid collected after filtration, and (e) the final purified product (HMS), with 5 mM DMSO used as an internal standard.

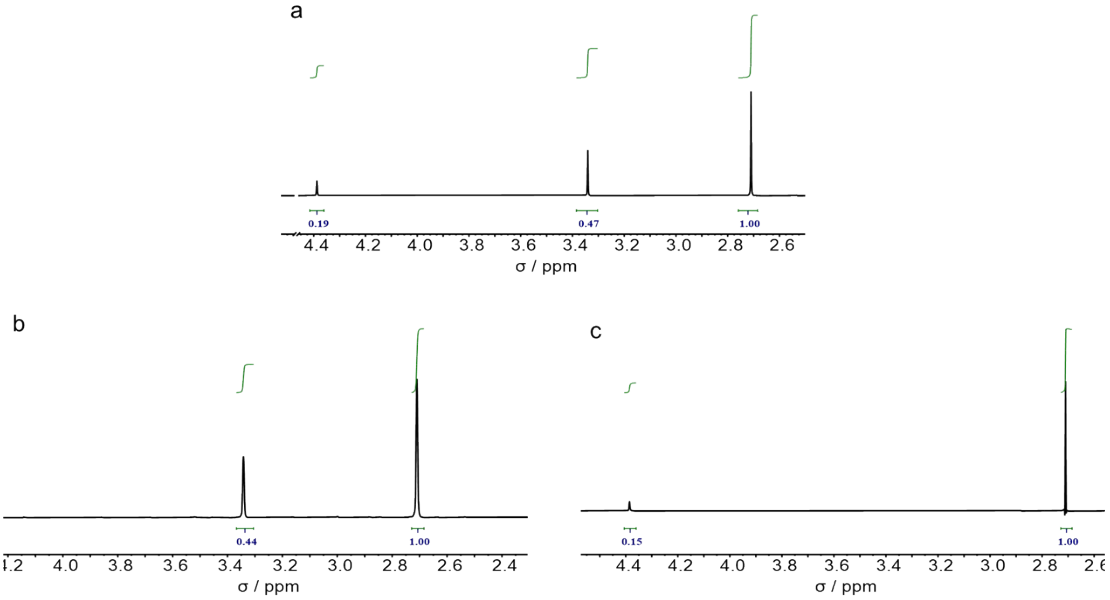

Figure S31**.** Truncated ^{1}H NMR spectra of the electrolyte after electrolysis (a), purified methanol (b) and HMS (c) after dilution to 100 mL. The separation yield of HMS: $\eta_{HMS} = \frac{0.15}{0.19} \times 100\% = 79\%$; The separation yield of MeOH: $\eta_{MeOH} = \frac{0.44}{0.47} \times 100\% = 94\%$.

Specifically, the separated HMS and methanol solution were diluted with water to a final volume of 100 mL and subjected to quantitative ^{1}H NMR analysis (Figure S38). The separation yields, based on a comparison of the concentration before and after the separation process, were 79% for HMS and 94% for methanol.

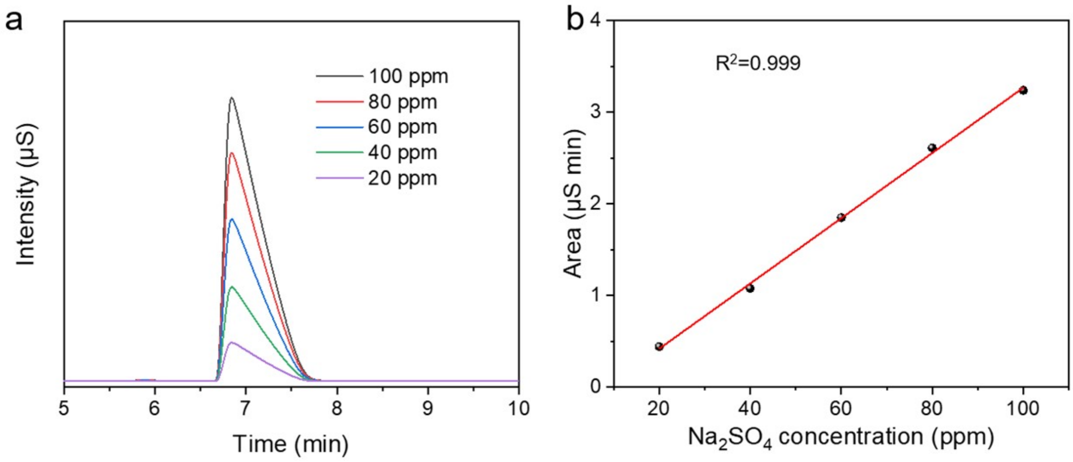

Figure S32. Calibration curve of Na_2SO_4 solution. (a) IC curves of Na_2SO_4 solutions with different concentrations. (b) The linear calibration relationship between the Na_2SO_4 concentration and corresponding peak area. Since Na_2SO_3 is easily oxidized to Na_2SO_4 in air, the purified electrolyte solid is pure Na_2SO_4 through IC test.

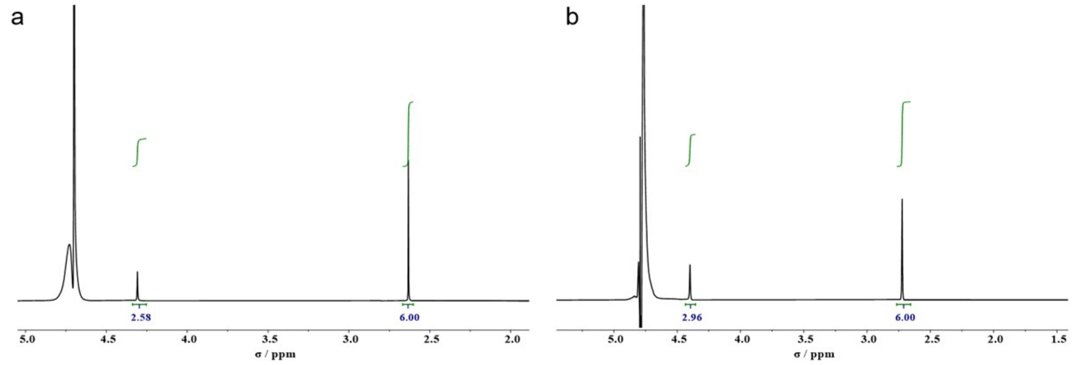

Figure S33. ^{1}H NMR of (a) purified HMS powder and (b) pure HMS powder. Samples preparation: 1 mg of purified or pure HMS powder was dissolved in 1 mL of water. A mixture of 200 μL of the resulting solution, 200 μL of 5 mM DMSO, and 100 μL of D_2O was used for the ^{1}H NMR analysis.

$$\text{Purity} = \frac{Integral\ area\ of\ purified\ HMS\ powder}{Integral\ area\ of\ pure\ HMS\ powder} \times 100 = \frac{2.58}{2.96} \times 100\% = 87.2\%$$

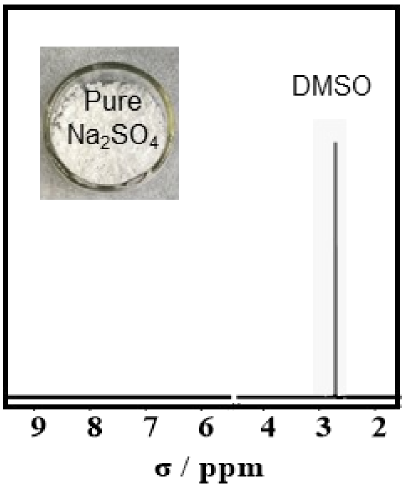

Figure S34. Partial ^{1}H NMR spectra of purified Na_2SO_4 solid with 5 mM DMSO used as an internal standard.

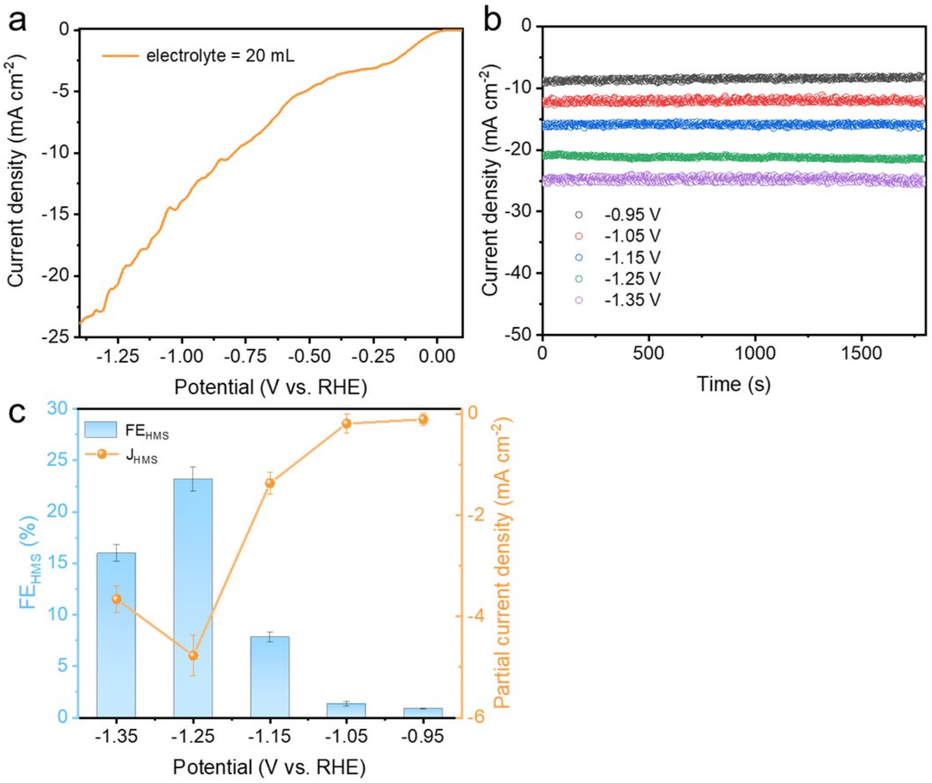

Figure S35. (a) LSV data, (b) i-t data as a function of applied potential and (c) FE and partial current density as a function of applied potential obtained for generation of HMS using a 1.0×1.0 cm^2 CoPc/CNT electrode in a 20 mL cathodic chamber.

The standard electrochemical cell employed a 10 mL cathodic chamber with a 1.0×1.0 cm^2 electrode. To evaluate the effect of electrolyte volume, electrolysis was performed in a larger H-cell with a 20 mL cathodic chamber while maintaining the same 1.0×1.0 cm^2 electrode. The maximum FE and partial current density for HMS were 23.2 ± 1.4% and -4.8 ± 0.4 mA cm^{-2}, respectively, which are comparable to those obtained in the standard configuration.

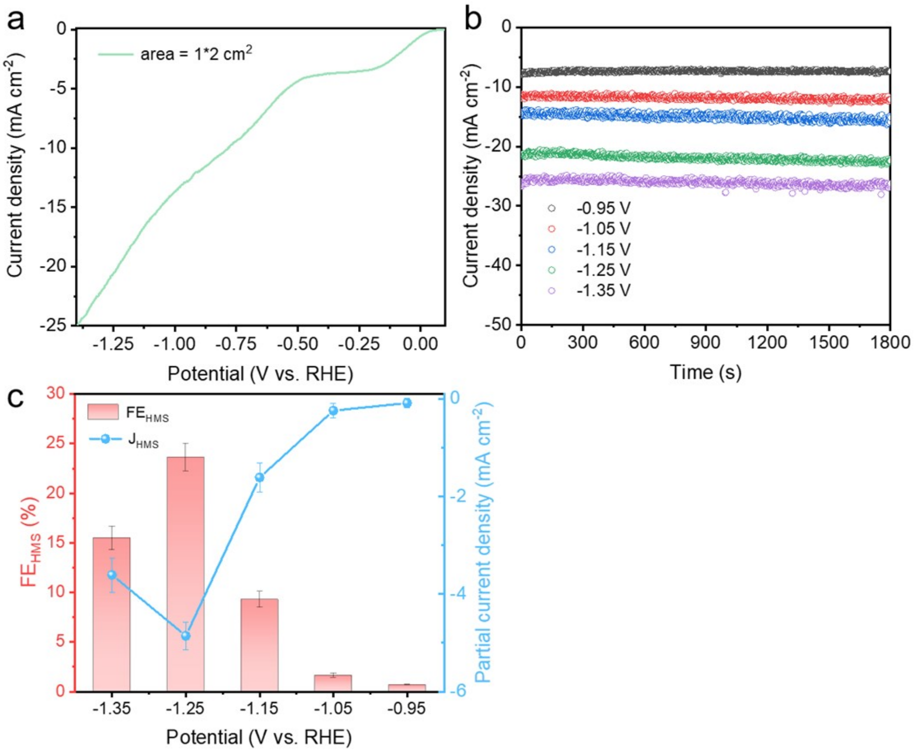

Figure S36. (a) LSV data, (b) i-t data as a function of applied potential and (c) FE and partial current density as a function of applied potential obtained for generation of HMS obtained using a 1.0×2.0 cm^2 CoPc/CNT electrode in a 10 mL cathodic chamber.

To probe the influence of electroactive surface area, a 1.0×2.0 cm^2 electrode was tested in the 10 mL cathodic chamber. The maximum FE and partial current density were 23.6 ± 1.4% and -4.9 ± 0.3 mA cm^{-2}, again showing negligible deviation from the baseline system.

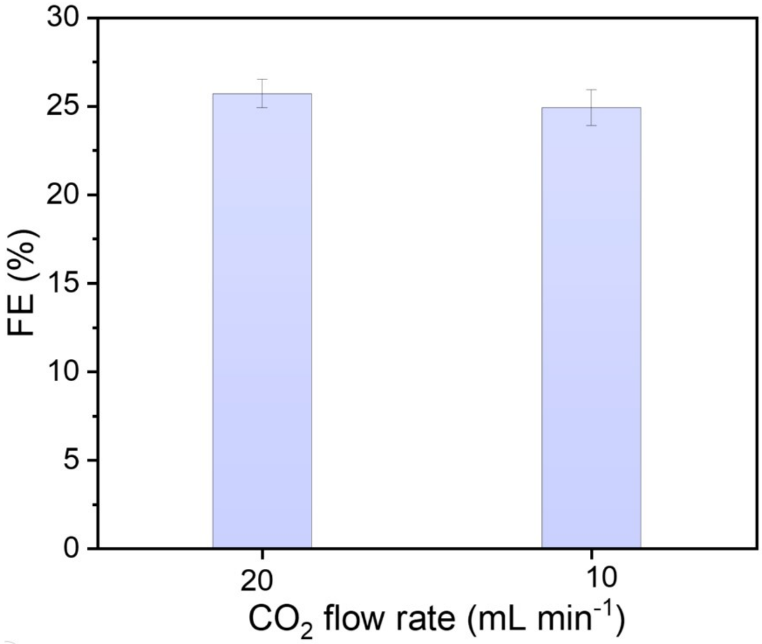

Figure S37. Effect of CO_2 flow rate on HMS formation.

To examine possible CO_2 mass transport limitations, the CO_2 flow rate varied from 20 mL min^{-1} to 10 mL min^{-1}. The FE for HMS formation remained essentially unchanged (24.9 ± 1.0 %) (Figure S37), indicating that CO_2 mass transport is not a dominant limiting factor.

Collectively, results demonstrate that HMS production from CO_2 and SO_3^{2-} with a CoPc/CNT electrode maintains stable electrocatalytic performance upon increasing electrolyte volume, enlarging electroactive area, and adjusting CO_2 flow rate, thereby supporting the feasibility of scale-up.

Table S3**.** Sustainability/Green metrics comparison between conventional and our methods.

Route	**Carbon Source**	**Sulfur Source**	**Hazard**	**Atom Economy**	**E-factor**
Conventional	Formaldehyde	SO_2	Toxic gas	~100%	~0 (theoretical); process-dependent in practice
This work	CO_2	SO_3^{2-}	Mild	86.10%	0.73 (FE-adjusted)*

*FE-adjusted E-factor calculated based on measured product distribution (HMS/CO/MeOH/H_2) and electron stoichiometry (HMS: 4e^-, CO:2e^-, MeOH:6e^-, H_2: 2e^-). Water was excluded by convention.

References

1. R. B. Gaussian 16, M. J. Frisch, G. W. Trucks, H. B. Schlegel, G. E. Scuseria, M. A. Robb, J. R. , G. S. Cheeseman, V. Barone, G. A. Petersson, H. Nakatsuji, X. Li, M. Caricato, A. V. Marenich, , B. G. J. J. Bloino, R. Gomperts, B. Mennucci, H. P. Hratchian, J. V. Ortiz, A. F. Izmaylov, J. , D. W.-Y. L. Sonnenberg, F. Ding, F. Lipparini, F. Egidi, J. Goings, B. Peng, A. Petrone, T. , D. R. Henderson, V. G. Zakrzewski, J. Gao, N. Rega, G. Zheng, W. Liang, M. Hada, M. Ehara, , R. F. K. Toyota, J. Hasegawa, M. Ishida, T. Nakajima, Y. Honda, O. Kitao, H. Nakai, T. Vreven, , J. A. M. K. Throssell, Jr., J. E. Peralta, F. Ogliaro, M. J. Bearpark, J. J. Heyd, E. N. Brothers, , V. N. S. K. N. Kudin, T. A. Keith, R. Kobayashi, J. Normand, K. Raghavachari, A. P. Rendell, , S. S. I. J. C. Burant, J. Tomasi, M. Cossi, J. M. Millam, M. Klene, C. Adamo, R. Cammi, J. , R. L. M. W. Ochterski, K. Morokuma, O. Farkas, J. B. Foresman, and D. J. Fox, Gaussian, Inc., and W. CT, 2016.

2. Y. Zhao and D. G. Truhlar, A new local density functional for main-group thermochemistry, transition metal bonding, thermochemical kinetics, and noncovalent interactions, *J. Chem. Phys.*, 2006, **125**, 194101.

3. M. Dolg, U. Wedig, H. Stoll and H. Preuss, Energy-adjusted ab initio pseudopotentials for the first row transition elements, *J. Chem. Phys.*, 1987, **86**, 866–872.

4. A. Bergner, M. Dolg, W. Küchle, H. Stoll and H. Preuß, Ab initio energy-adjusted pseudopotentials for elements of groups 13–17, *Mol. Phys.*, 1993, **80**, 1431–1441.

5. P. C. Hariharan and J. A. Pople, The influence of polarization functions on molecular orbital hydrogenation energies, *Theor. Chim. Acta*, 1973, **28**, 213–222.

6. F. Weigend, F. Furche and R. Ahlrichs, Gaussian basis sets of quadruple zeta valence quality for atoms H–Kr, *J. Chem. Phys.*, 2003, **119**, 12753–12762.

7. A. V. Marenich, C. J. Cramer and D. G. Truhlar, Universal Solvation Model Based on Solute Electron Density and on a Continuum Model of the Solvent Defined by the Bulk Dielectric Constant and Atomic Surface Tensions, *J. Phys. Chem. B*, 2009, **113**, 6378–6396.

8. T. Lu and F. Chen, Multiwfn: A multifunctional wavefunction analyzer, *J. Comput. Chem.*, 2012, **33**, 580–592.

9. F. Neese, The ORCA program system, *WIRES Comput. Molec. Sci.*, 2012, **2**, 73–78.

10. F. Neese, Software update: The ORCA program system—Version 5.0, *WIRES Comput. Molec. Sci.*, 2022, **12**, e1606.

11. S. Grimme, J. G. Brandenburg, C. Bannwarth and A. Hansen, Consistent structures and interactions by density functional theory with small atomic orbital basis sets, *J. Chem. Phys.*, 2015, **143**, 054107.

12. J. Hutter, M. Iannuzzi, F. Schiffmann and J. VandeVondele, cp2k: atomistic simulations of condensed matter systems, *WIRES Comput. Molec. Sci.*, 2014, **4**, 15–25.

13. J. VandeVondele and J. Hutter, Gaussian basis sets for accurate calculations on molecular systems in gas and condensed phases, *J. Chem. Phys.*, 2007, **127**, 114105.

14. S. Goedecker, M. Teter and J. Hutter, Separable dual-space Gaussian pseudopotentials, *Phys. Rev. B*, 1996, **54**, 1703–1710.

15. S. Grimme, S. Ehrlich and L. Goerigk, Effect of the damping function in dispersion corrected density functional theory, *J. Comput. Chem.*, 2011, **32**, 1456–1465.

16. S. Grimme, C. Bannwarth and P. Shushkov, A robust and accurate tight-binding quantum chemical method for structures, vibrational frequencies, and noncovalent interactions of large molecular systems parametrized for all spd-block elements (Z = 1–86), *J. Chem. Theory Comput.*, 2017, **13**, 1989–2009.

17. W. Humphrey, A. Dalke and K. Schulten, VMD: Visual molecular dynamics, *J. Mol. Graph.*, 1996, **14**, 33–38.

18. M. A. Kline, M. H. Barley and T. J. Meyer, Electrocatalytic reduction of bisulfite to hydrogen sulfide based on a water-soluble iron porphyrin, *Inorg. Chem.*, 1987, **26**, 2196–2197.

19. S.-M. Chen and S.-W. Chiu, The electrocatalytic transformation of HS^{-}, $S_2O_3^{2-}$, $S_4O_6^{2-}$ and SO_3^{2-} to SO_4^{2-} by water-soluble iron porphyrins, *Electrochim. Acta*, 2000, **45**, 4399–4408.

20. A. Singh, A. Zamader, R. Khakpour, K. Laasonen, M. Busch and M. Robert, Molecular Electrochemical Catalysis of CO-to-Formaldehyde Conversion with a Cobalt Complex, *J. Am. Chem. Soc.*, 2024, **146**, 22129–22133.